Investigation of Incompressible Dynamic Stall Physics by Application of a Parametric Proper Orthogonal Decomposition

Dustin G. Coleman* Flint O. Thomas [†] Stanislav Gordeyev [‡]

Kyle C. Heintz * Thomas C. Corke [§]

Institute for Flow Physics and Control

University of Notre Dame, Notre Dame, IN, 46556, USA

Nomenclature

a_∞	Freestream speed of sound, m/s
c	Chord length, m
f	Pitch frequency, Hz
k	Reduced frequency, $\pi f c/U_\infty$
M_∞	Freestream Mach number, U_∞/a_∞
q	Freestream dynamic pressure, $1/2\rho_\infty U_\infty^2$
Re_c	Reynolds number based on airfoil chord, $U_\infty c/\nu$
s	Span length, m
t	Time, s
u'	Fluctuating velocity, m/s
U_∞	Freestream flow speed, m/s
α	Angle of attack, deg.
α_0	Mean angle of attack, deg.
α_1	Pitch oscillation amplitude, deg.
ρ	Density, kg/m^3
ω	Circular frequency, rad/s

Subscript

cg	Center of gravity
∞	Freestream

I.   Introduction

The unsteady flow phenomenon known as dynamic stall occurs as an airfoil rapidly exceeds its static stall angle of attack, α_{ss}, resulting in the production of nonlinear, and often detrimental, airloads. As the airfoil continues to pitch up, vorticity accumulates near the leading edge. Ultimately the boundary layer breaks down leading to the subsequent formation of the most salient feature of the process: a coalesced structure termed the dynamic stall vortex (DSV). Upon its formation, the DSV grows in strength, detaches

---

*Graduate Research Assistant, Aerospace and Mechanical Engineering, University of Notre Dame, and AIAA Student Member.

[†]Professor, Aerospace and Mechanical Engineering, University of Notre Dame, AIAA Associate Fellow.

[‡]Research Associate Professor, Aerospace and Mechanical Engineering, University of Notre Dame, AIAA Associate Fellow.

[§]Professor, Aerospace and Mechanical Engineering, University of Notre Dame, AIAA Fellow.

American Institute of Aeronautics and Astronautics

from the surface, and propagates aft over the airfoil where it is finally ejected into the wake, initiating a fully separated region over the lifting surface. This process results in the development of hysteresis loops in the aerodynamic loads, which experience large excursions from their static values. Consequently, the fatigue life of many components is quickly consumed. Comprehensive reviews of the phenomenon are given by McCroskey,[11] Carr,[2] and Leishman.[7]

Despite dynamic stall being the topic of an extensive amount of research over previous decades, the unsteady event remains to be fully understood, particularly the dynamics involving its initiation. Ericsson and Reding stated that, "only if the unsteady stall mechanism is understood can an 'analytic extrapolation' to full scale [rotors] be made with confidence,"[4] conveying the importance and difficulty of successfully predicting the unsteady process. In this paper, measured surface pressures, which are a function of both space and time, are expressed in terms of a parametric proper orthogonal decomposition (PPOD) in order to obtain an optimum (in the mean-square sense) modal representation of the unsteady surface pressure. In this manner, a modal decomposition of unsteady lift and quarter-chord moment is also obtained for both "light" and "deep" stall cases. This provides a systematic and quantitative framework by which to elucidate common and disparate features of the light and deep dynamic stall processes and provides a bridge to the development of low-order models.

II.   Proper Orthogonal Decomposition

A spectral decomposition of a signal $u = u(x, t)$ using POD results in an optimal set of spatial modes, based on energy, yielding a series representation of the form

$$u(x, t) = \sum_i a_i(t)\phi_i(x), \tag{1}$$

where $a_i(t)$ are temporal coefficients describing the dynamic behavior of each spatial mode, $\phi_i(x)$.[8] The resulting empirical modes represent the original signal better than those determined by any other bases of the same dimension, thus requiring only a minimum number of modes to appropriately reconstruct the original function. The modes are derived by maximizing the function

$$I = \frac{\langle |(u, \phi)|^2 \rangle}{||\phi||^2}, \tag{2}$$

where $(\cdot, \cdot)$ is an inner product for the $L^2(\Omega_x)$ space of square-integrable functions and $|| \cdot ||$ is the norm of the space using the given the inner product. The inner product is defined as

$$(f, g) = \int_{\Omega_x} (f \cdot g^*) \mathrm{d}x, \tag{3}$$

resulting in a squared norm of the form

$$||\phi||^2 = (\phi, \phi) = \int_{\Omega_x} \phi^2 \mathrm{d}x, \tag{4}$$

where Ω_x is the domain over which u and ϕ are defined. In Eq. 2, $\langle \cdot \rangle$ is an averaging operator over the time domain. Using variational calculus and the definitions in Eq. $3 - 4$, the optimization problem of Eq. 2 can be cast into the integral eigenvalue problem

$$\int_{\Omega_x} \langle u(x) \cdot u(x') \rangle \phi^*(x') \mathrm{d}x' = \lambda \phi(x), \tag{5}$$

where $\langle u(x) \cdot u(x') \rangle = R(x, x')$ is the temporally averaged autocorrelation function of $u(x, t)$ and λ is the corresponding eigenvalue.[6] Modes are prioritized according to their relative energy by comparing their respective eigenvalues: relative energy $= \lambda_i / \sum_j \lambda_j$. Once the modes are determined, the temporal coefficients, $a_i(t)$, are found by projecting the original function, $u(x, t)$, onto the modes, $\phi_i(x)$, i.e.

$$a_i(t) = \int_{\Omega_x} (u(x, t) \cdot \phi_i(x)) \mathrm{d}x. \tag{6}$$

American Institute of Aeronautics and Astronautics

POD was originally proposed by Lumley[8] as a means of determining coherent structures in presumably random turbulent fields. Likewise, it has been used extensively in the analysis of particle imaging velocimetry (PIV) data sets to determine the most fundamental features of given flow fields. Recently, Gordeyev and Thomas[5] introduced a new POD technique to capture the dynamics of a flow field having two distinct characteristic states. This technique determined optimal modes for each flow state as well as the transients existing from the trajectories between the two states. While this technique was applied to a study of flow control, it offers a means of determining characteristic modes of multi-parameter functions, such as the flow field events associated with dynamic stall. Considering then a function of multiple parameters, such as the surface pressure field of an airfoil during a dynamic stall event, the eigenvalue problem from Eq. 5 becomes

$$\int R(\xi, \xi'; k, \alpha_0, \alpha_1)\phi_i(\xi'; k, \alpha_0, \alpha_1)\mathrm{d}\xi' = \lambda_i(k, \alpha_0, \alpha_1)\phi_i(\xi; k, \alpha_0, \alpha_1), \qquad ||\phi_i||^2 = 1, \tag{7}$$

where the eigenvectors and eigenvalues are now contained within subsets of reduced frequency k, mean angle of attack α_0, and pitch oscillation amplitude α_1. Here, the spatial coordinate is the non-dimensional chord-wise location, $\xi = x/c$. The modes are also restricted to be orthonormal. The pressure field is then reconstructed in the low-dimensional space spanned by the eigenvectors as in Eq. 1,

$$p(\xi, \alpha; k, \alpha_0, \alpha_1) = \sum_i b_i(\alpha; k, \alpha_0, \alpha_1)\phi_i(\xi; k, \alpha_0, \alpha_1). \tag{8}$$

To further extract common features of the dataset, specifically the fundamental modes describing all subsets, it is desirable to obtain a set of purely spatial modes by applying POD to the $\phi-$modes as

$$\phi_i(\xi; k, \alpha_0, \alpha_1) = \sum_j d_{i,j}(k, \alpha_0, \alpha_1)\psi_{i,j}(\xi), \qquad ||\psi_{i,j}||^2 = 1. \tag{9}$$

The resulting $\psi-$modes are the optimal set of spatial modes describing the multiple subsets. As noted in reference,[5] the $\psi-$modes are also realized by first applying POD to the entire dataset *i.e.* all subsets of k, α_0, and α_1 lumped into a single set. This approach is termed parametric POD (PPOD) and is the technique used in this paper. The decomposition then takes a similar form to Eq. 1,

$$p(\xi, \alpha; k, \alpha_0, \alpha_1) = \sum_i a_i(\alpha; k, \alpha_0, \alpha_1)\psi_i(\xi), \qquad ||\psi_i||^2 = 1. \tag{10}$$

III.   Experimental Setup

All experiments were conducted in the Mach 0.6 closed-return windtunnel located at the University of Notre Dame. A top-down view of the windtunnel is shown in Figure 1 along with many of its key features. The flow is driven by a 1750 h.p. variable rpm AC motor that turns an 8 ft diameter, high solidity, 2-stage fan. At a given flow speed, equilibrium temperature is achieved by actively cooling the turning vanes downstream of the fan via 40° F water. The flow is then conditioned by a 5 in. thick honeycomb wall (0.25 in. nominal diameter) followed by five #28 wire screens leading to a 6:1 contraction. The resulting turbulence intensity is around $u'/U_\infty = 0.05\%$, which is comparable to free-flight conditions.

The tunnel has three interchangeable test sections, of which, one has been retrofitted to accommodate unsteady, pitching airfoil experiments. The test section is depicted in Figure 2 along with the pitching mechanism. Airfoils are mounted between two 0.75 in. thick aluminum splitter plates and fixed to rotate about their quarter-chord position. Each side of the airfoil is fitted with a 0.5 in. thick Lexan end plate (rotating disk), which is housed inside the splitter plate and secured with an aluminum enclosure, creating a labyrinth seal. Instrumentation is carried out of the test section opposite the pitching mechanism, while the pitching motion is driven through the torque tube, connected to the mechanism. The torque tube and wire shaft are both supported by passing through ball bearings housed in aluminum casings, secured to the test section floor, found just outside of each splitter plate. The bearing houses facilitate the transmission of aerodynamic loads to the test section.

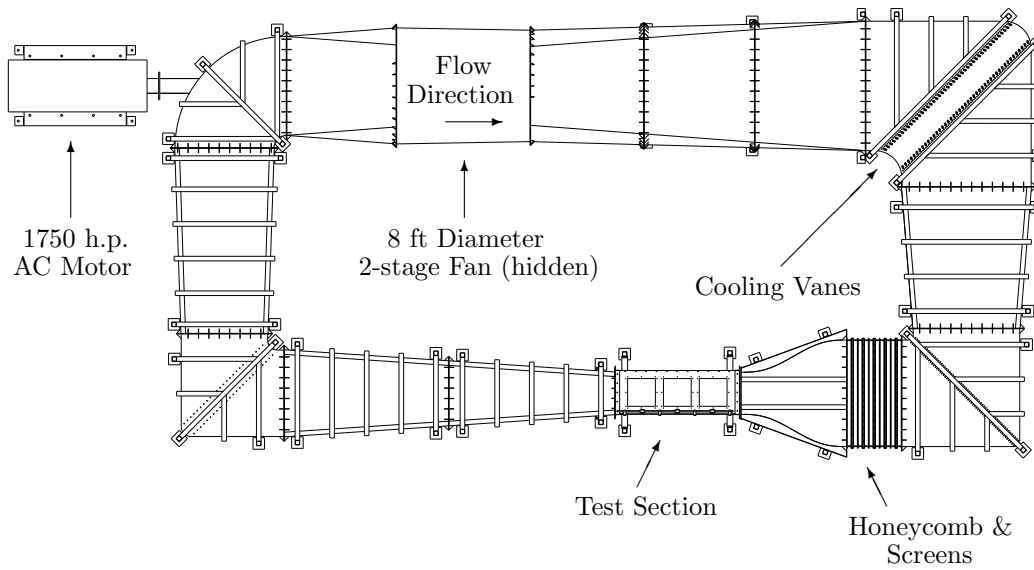American Institute of Aeronautics and Astronautics

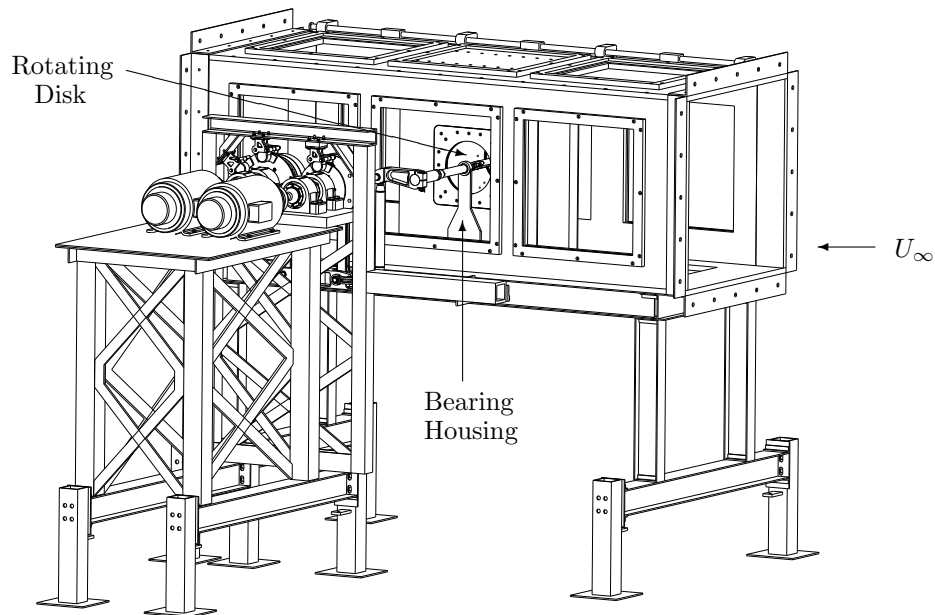Figure 1: University of Notre Dame Mach 0.6 windtunnel: top view

Figure 2: Dynamic stall test section and pitching mechanism

III.A. Airfoil

A NACA 23012 section profile was used as the airfoil in this experiment. The model was constructed from three high strength aluminum (Al 7075-t6) pieces. This design facilitated the proper installation of pressure

transducers and safe storage of transducer cables while maintaining a rigid housing with hydrodynamically smooth surfaces. To lower the inertial loading, improve the stability of the system, and provide wire paths, two large spanwise sections were removed from the internal mass. Consequently, the center of gravity was fixed at $x/c_{cg} = 0.425$. The model chord length was set at $c = 0.254$ m (10 in.) and had a span of $s = 0.3556$ m (14 in.) in order to operate in the facility as previously described. The model is depicted in Figure 3, showing the spanwise cutouts, wire storage, and instrumentation installation.
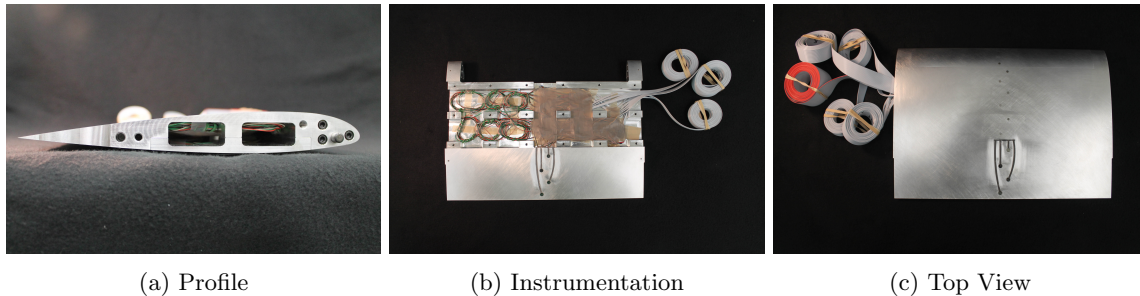

| (a) Profile | (b) Instrumentation | (c) Top View |

Figure 3: NACA 23012 model

Surface pressure was measured along the midspan using 31 high frequency response, absolute pressure transducers manufactured by Kulite and Endevco. The transducers were positioned along the chord using a cosine distribution described as

$$x_n/c = 1 - \cos\left(\frac{n\pi}{2N}\right), \tag{11}$$

where $N = 15$, $n = 0, 1, ..., N - 1$, and x_n/c is the non-dimensional chord station of the pressure transducer. The last pressure port was located at $x_{15}/c = 0.975$ due to the thickness of the sensor and the sharp trailing edge of the airfoil.

III.B.   Data Acquisition

The analog pressure signals were low-pass, anti-alias, filtered at 2500 Hz before being amplified and offset to provide the highest signal-to-noise ratio possible. All pressure (freestream and surface) and angle of attack signals were then digitized at a sampling frequency of $f_s = 5000$ Hz by a Microstar Laboratories DAP5380a and three MSXB 028 simultaneous sampling boards, which offer 12-bit resolution.

III.C.   Pitching Mechanism

The unique pitching mechanism is a dual-input walking beam design that allows two-degree-of-freedom motion on the pitch output. A detailed, labeled view of the pitch mechanism is shown in Figure 4. The adjustable pitch link is used to control the mean angle of attack, α_0, by varying its length. Oscillation amplitude provided by each flywheel input is controlled by offsetting the respective spindle placement from the center using the Acme threads. The walking beam acts as a mechanical adder of the two frequency and amplitude inputs from the two flywheels, to produce complex pitching trajectories at the torque tube connection. Each flywheel is driven by a Marathon 10 hp Black Magic 420 VAC motor. Dynapar internal encoders monitored by Yaskawa F-7 drives provide rpm control independently for each motor. For the purposes of this experiment, only single frequency pitch motions were considered.

IV.   Results

The parameters dictating the airfoil pitching trajectories and the free stream flow conditions are summarized in Table 1. The pitching trajectories were chosen to coincide with the regimes used to characterize the severity of dynamic stall: attached flow pitching, stall onset, light stall, and deep stall. These regimes

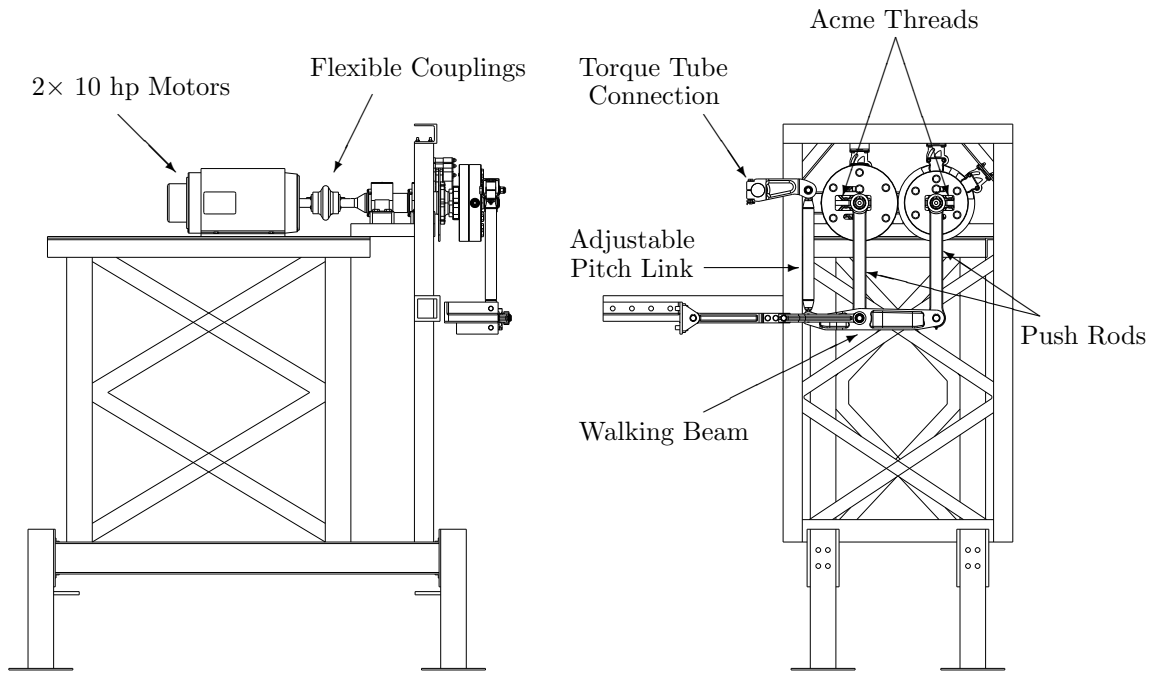American Institute of Aeronautics and Astronautics

Figure 4: Pitching mechanism detail

classify the maturation of the leading edge vortex during the dynamic stall process as shown in Figure 5. For a more in depth description refer to McCroskey $et\ al$[9] or McCroskey and Pucci.[10]

Table 1: Pitch Motion Characteristics

Parameter		Value
Free stream Mach #, M_∞	$=$	0.2
Reduced frequency, k	$=$	0.05, 0.075, 0.1
Mean angle of attack, α_0	$=$	5°, 8°, 13°
Oscillation amplitude, α_1	$=$	10°

The integrated aerodynamic normal force and quarter-chord moment used for the following analysis are defined, respectively, as:

$$C_n = \int\limits_0^1 \left(C_p^P - C_p^S \right) \mathrm{d}\xi, \tag{12}$$

$$C_m = -\int\limits_0^1 \left(C_p^P - C_p^S \right) \xi \mathrm{d}\xi + C_n/4, \tag{13}$$

where C_p^P and C_p^S are the respective bottom (pressure) side and top (suction) side non-dimensional pressure coefficients.
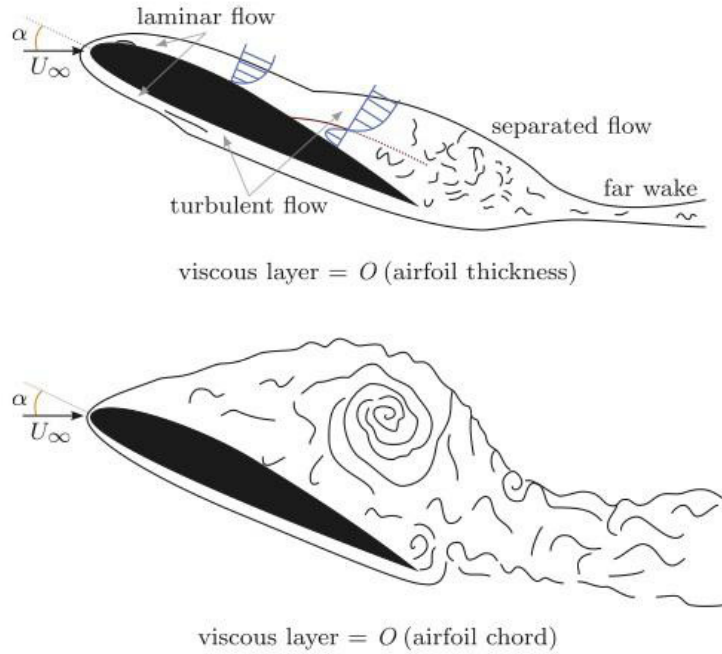
American Institute of Aeronautics and Astronautics

Figure 5: Flow behavior in the light (top) and deep (bottom) stall regimes[10]

IV.A.   Moving to a Suitable Reference Frame

To discern the dynamics of the surface pressure field associated with the unsteady flow over the airfoil, a change of reference frame is considered. Namely, the steady, inviscid pressure field for each respective angle of attack is removed from the experimental dataset. The steady, inviscid surface pressure is provided via a Hess-Smith panel method[3] written in MATLAB. Figure 6 shows a comparison of the non-dimensional chord-wise surface pressure acquired from the experimental dataset and the steady, inviscid panel method. The case shown represents a quasi-steady, attached flow pitching trajectory. Because of the quasi-steady nature of the pitching, the experimental pressure field should be free from significant unsteady delays and, therefore, the panel method should provide a rather accurate description. However, it can be seen in Figure 6 that the experimental pressure field is bounded by the panel method solution resulting in a smaller integrated normal force, C_n, of the former when compared to the latter. This point is shown more completely in Figure 7 where the slope of C_n for the experimental data is much lower than the computed inviscid value. The discrepancy is likely due to the tunnel blockage calibration. For comparison sake, the panel method pressures were scaled by 0.8 resulting in a comparable pressure field to the experimental data based on the integrated normal force values as shown by the red line in Figure 7.

The steady, inviscid pressure field supplied by the scaled panel method is removed from the experimental dataset, leaving the unsteady, viscous pressures defined as

$$C_p^* = C_{p,exp} - C_{p,panel}, \tag{14}$$

where the subscript exp stands for experimental data and $panel$ for panel method data. By moving to this reference frame, the PPOD analysis produces spatial modes of the C_p^* function that represent, by definition, perturbations from the steady, inviscid pressure field, which is known given the angle of attack and the airfoil shape.
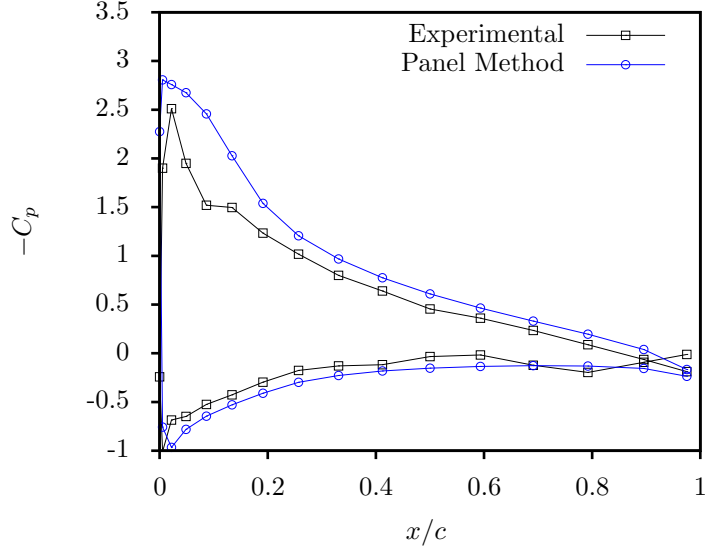
American Institute of Aeronautics and Astronautics

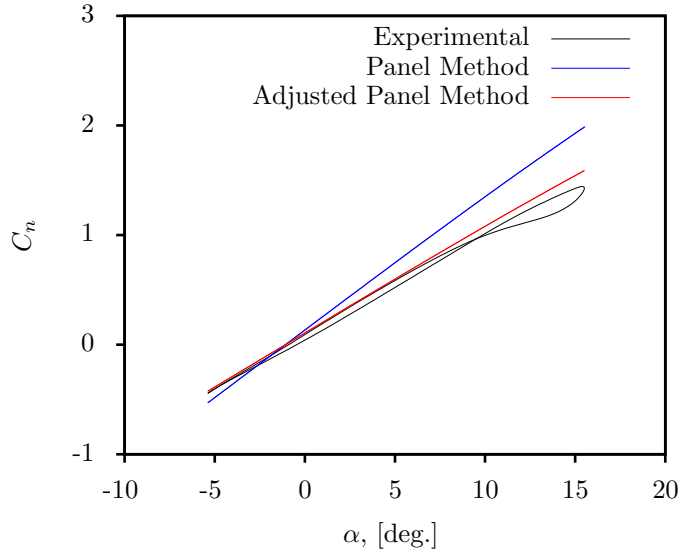Figure 6: Comparison of $-C_p$ at $\alpha = 8°$ for $k = 0.05$, $\alpha_0 = 5°$ pitching case

Figure 7: Comparison of C_n for $k = 0.05$, $\alpha_0 = 5°$ pitching case

IV.B.   Parametric POD Modes

Using the decomposition described in Eq. 10, the dataset of $C_p^*(\xi, \alpha; k, \alpha_0, \alpha_1)$ for all cases composed of attached flow pitching, light stall, and deep stall was decomposed into $\psi-$ spatial modes and their corresponding dynamic coefficients, a_i. One metric for assessing the significance of each mode is to compare its respective eigenvalue, representing the modal energy, from Eq. 7 to the summed total of all the eigenvalues resulting in a contribution percentage. Figure 8 depicts the magnitude of the each mode's eigenvalue in log scale on the left abscissa while showing the cumulative contribution percentages on the right abscissa, which exhibits a rapid convergence. This convergence behavior suggests that relatively few modes are required to adequately reconstruct the surface pressure field. In fact, after only five modes the cumulative energy contribution percentage is 99.9%.

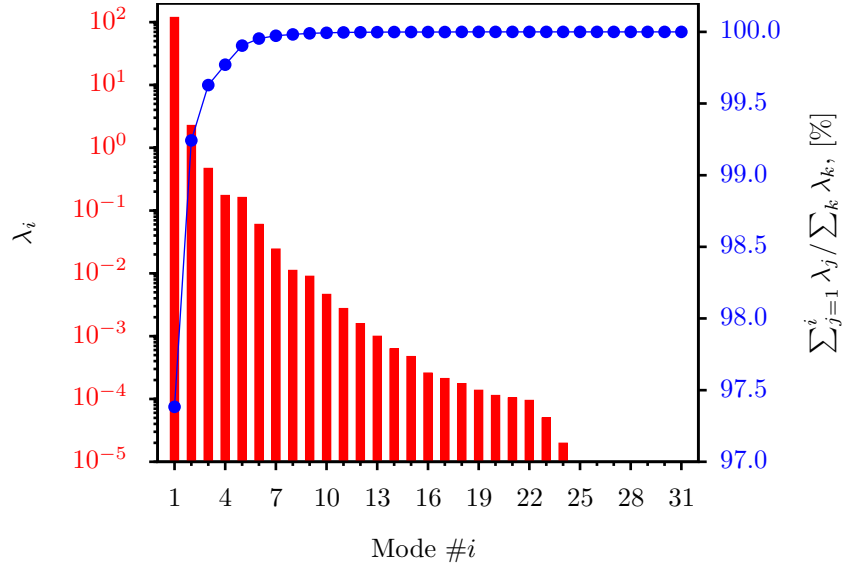American Institute of Aeronautics and Astronautics

Figure 8: Eigenvalue convergence

Figure 9 shows the first five modes of the decomposition as a function of the non-dimensional spatial coordinate, ξ. Here, negative and positive spatial coordinates refer to the bottom (pressure) side and the top (suction) side of the airfoil, respectively. The leading edge coordinate is $\xi = 0$ with $|\xi| = 1$ corresponding to the trailing edge. The respective dynamic coefficients, a_i, for each spatial mode displayed in Figure 9 are shown in Figure 10 as functions of angle of attack, α, and are organized in columns of reduced frequency, k. The subfigures show the dynamic response of each respective spatial mode for attached flow pitching (red), light stall (blue), and deep stall (black). Each modal response is shown as a phase average with error bars representing the standard deviation of the function at each phase location.

To evaluate the robustness of the PPOD reconstruction, a comparison with the integrated aerodynamic loads is considered. Similar to the surface pressure field, the unsteady, viscous aerodynamic loads used for comparison are defined as

$$C_n^* = C_{n,exp} - C_{n,panel}, \tag{15}$$

$$C_m^* = C_{m,exp} - C_{m,panel}. \tag{16}$$

The non-dimensional load differences being compared are the normal force, C_n^*, and the quarter-chord pitching moment, C_m^*, because of their importance to the rotor dynamicist when developing airfoil sections. The equivalent aerodynamic loading values for the PPOD reconstruction are determined as

$$C^*_{\substack{n,i \\ PPOD}} = a_i \int_0^1 \left(\psi_i^+(\xi) - \psi_i^-(\xi) \right) \mathrm{d}\xi, \tag{17}$$

$$C^*_{\substack{m,i \\ PPOD}} = -a_i \int_0^1 \left(\psi_i^+(\xi) - \psi_i^-(\xi) \right) \xi \mathrm{d}\xi + C^*_{\substack{n,i \\ PPOD}} /4, \tag{18}$$

where the superscript on ψ represents the suction side $(+)$ or pressure side $(-)$ of the airfoil as in Figure 9. To quantify the error of the PPOD approximation with respect to the experimental data, the following definition is used:
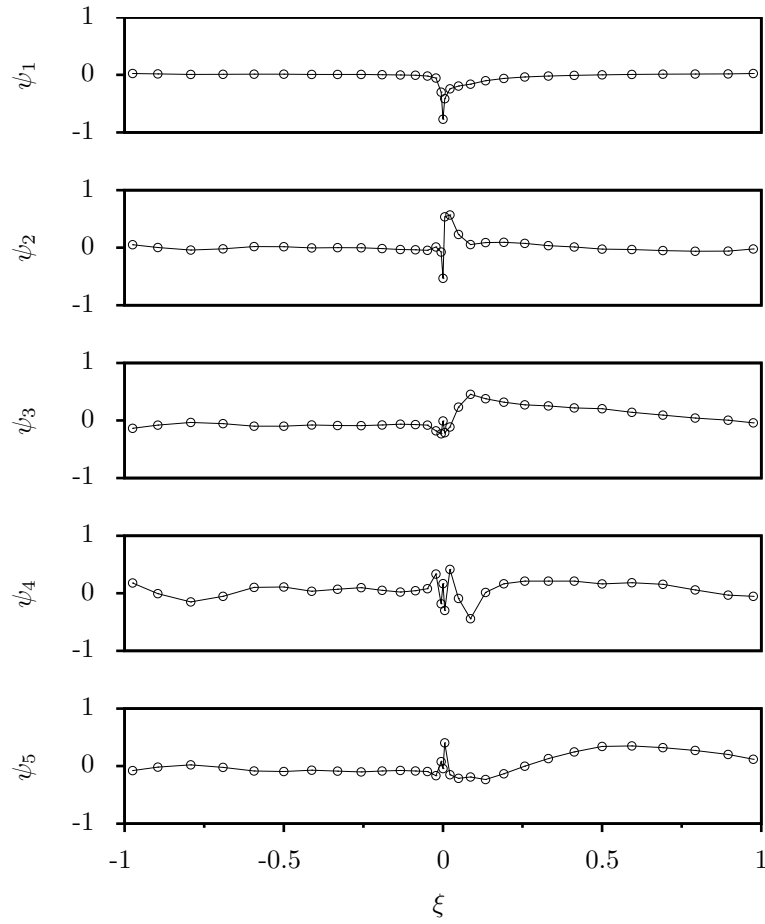
American Institute of Aeronautics and Astronautics

Figure 9: First five $-C_p^*$ mode shapes, ψ_i

American Institute of Aeronautics and Astronautics
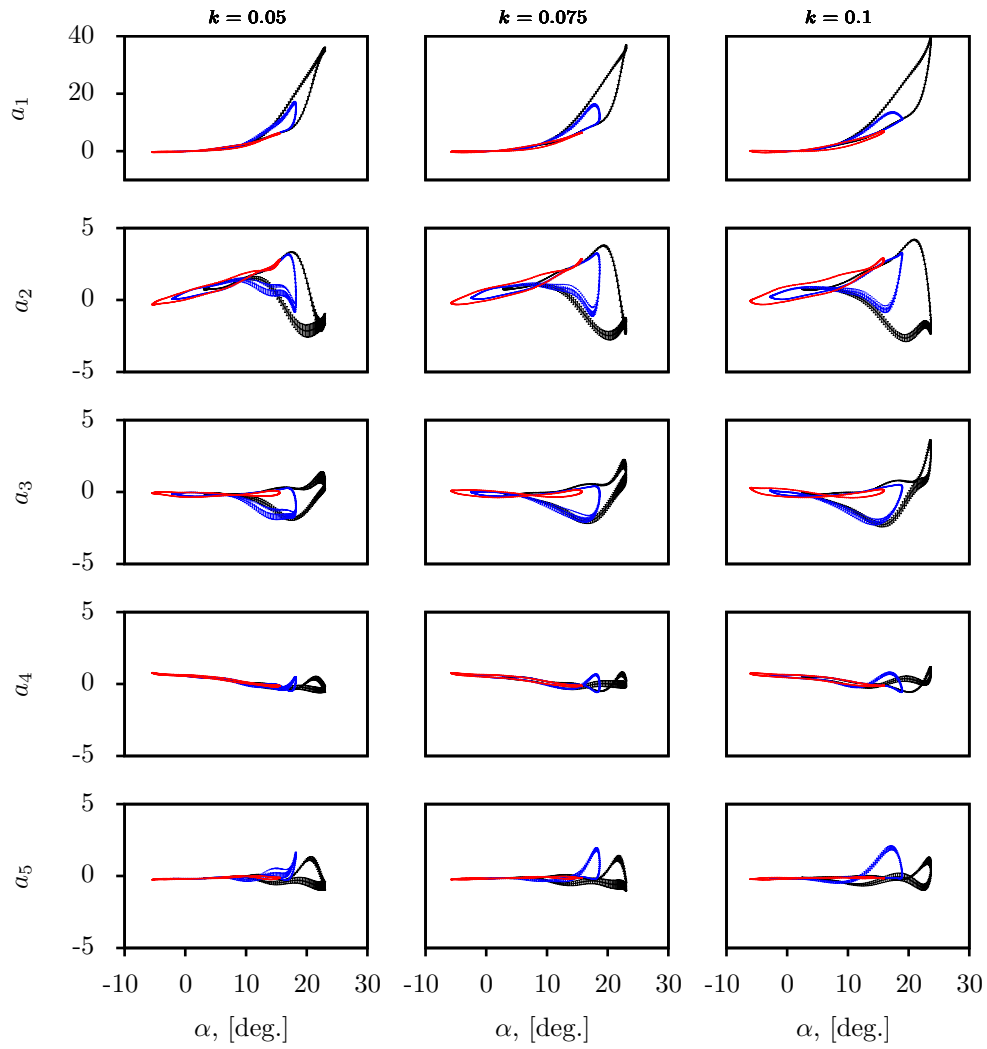
Figure 10: First five $-C_p^*$ modal coefficients, a_i:
$\alpha_0 = 5°$ ⊥ , $\alpha_0 = 8°$ ⊥ , $\alpha_0 = 13°$ ⊥

American Institute of Aeronautics and Astronautics

$$\text{Relative Error} = \frac{\sum \left(\langle C_x^* \rangle - \langle \sum\limits_{i=1}^{j} C_{x,i}^* \rangle_{PPOD} \right)^2}{\left(\max(\langle C_x^* \rangle) - \min(\langle C_x^* \rangle) \right)^2}, \tag{19}$$

where $\langle \cdot \rangle$ is the phase averaging operator, j is the current number of modes used for the approximation, and the denominator represents the square of the maximum range of the experimental signal.

PPOD approximations using up to five modes and their resulting relative errors (denoted $R.E.$) are shown in Figure 11 and Figure 12 for C_n^* and C_m^*, respectively. The columns of these figures represent trajectories indicative of attached flow (quasi-steady) pitching, light stall, and deep stall with their pitching parameters defined in Table 2. These pitching cases were chosen to demonstrate how the PPOD reconstructions behave across a range of reduced frequencies and mean angles of attack, and thus, will serve as the trajectories considered for the remainder of the analysis. The phase averaged values of the experimental data are shown in black with error bars representing the standard deviation at each respective phase location. Likewise, the red lines are the phase averaged PPOD approximations.

Table 2: Comparison Cases

Case Type	Parameters
Attached Flow	$k = 0.05$, $\alpha_0 = 5°$
Light Stall	$k = 0.075$, $\alpha_0 = 8°$
Deep Stall	$k = 0.1$, $\alpha_0 = 13°$

Globally, the results indicate that the relative error for C_m^* is typically higher than that of C_n^* for the same respective reconstruction, which suggests a sensitivity of the pressure distribution on the calculation of the integrated moment. The addition of each mode generally reflects an improvement in the qualitative shape of the approximations. Once the first five modes are used the relative error exhibits large reductions, and the approximated trajectories nearly lie on top of the experimental data for all cases. This level of approximation also captures the correct magnitude of the moment stall (Figure 12) and the sudden increase in lift preceding lift stall ($k = 0.1$, $\alpha_0 = 13°$ case of Figure 11). While physical interpretations of the mode shapes will not be made here, a summary of their influence on the approximations is provided as follows:

Mode 1: This mode tends to capture the general behavior of the lift and moment curves with the exception of the $k = 0.05$, $\alpha_0 = 5°$ moment. The approximated lift curves show little deviation from the experimental lift at low angles of attack, while the dominant trend of stall and hysteresis is realized at higher angles. The same can be said of the moment trajectories, however, the attached flow pitching approximation appears to anticipate stalled behavior at higher angles of attack. Generally, mode 1 provides the global trend for each load response approximation, which is further corrected by the addition of succeeding modes.

Mode 1-2: The first correction is made by the second mode, shifting the upstroke values of each approximation towards the correct experimental values. In each case the upstroke values are significantly improved, resulting in a reduction of the relative error. The lift approximation of the $k = 0.05$, $\alpha_0 = 5°$ case sees an increase in relative error because the approximation does not account for the slight hysteresis effects. The shapes of mode 1 and mode 2 in Figure 9 seem to suggest that these two modes are complimentary in controlling the peak suction pressure on the leading edge.

Mode 1-3: The lift stall response is better captured once mode 3 is added to the reconstruction. Here, large reductions in the lift relative error are realized. However, the moment response only sees slight reductions in relative error. This result could be due to the fact that while the shape of mode 3 does exhibit a suction pressure field that is distributed more evenly over the upper surface of the airfoil, the
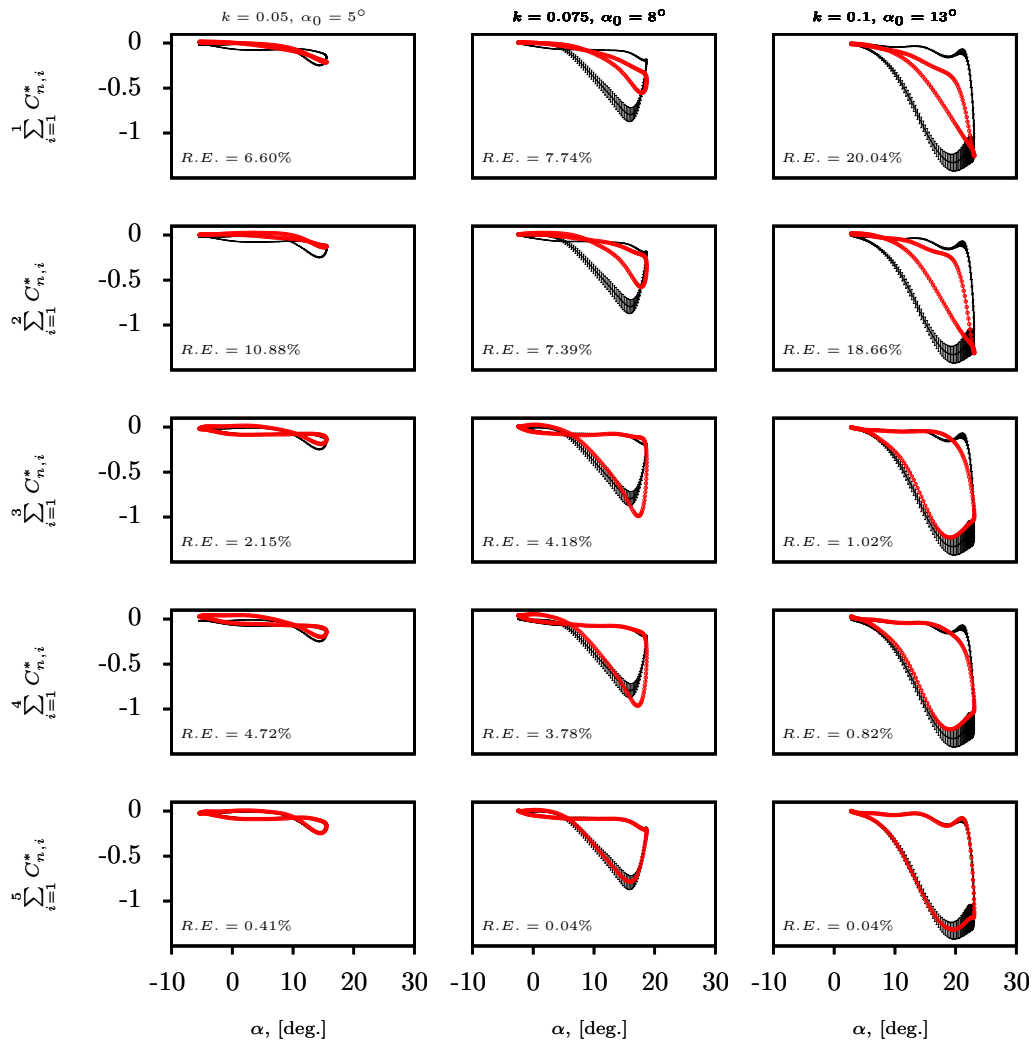
Figure 11: Comparison of actual C_n^* to PPOD approximation of C_n^*:
Experiment ⊥ , PPOD ⊸

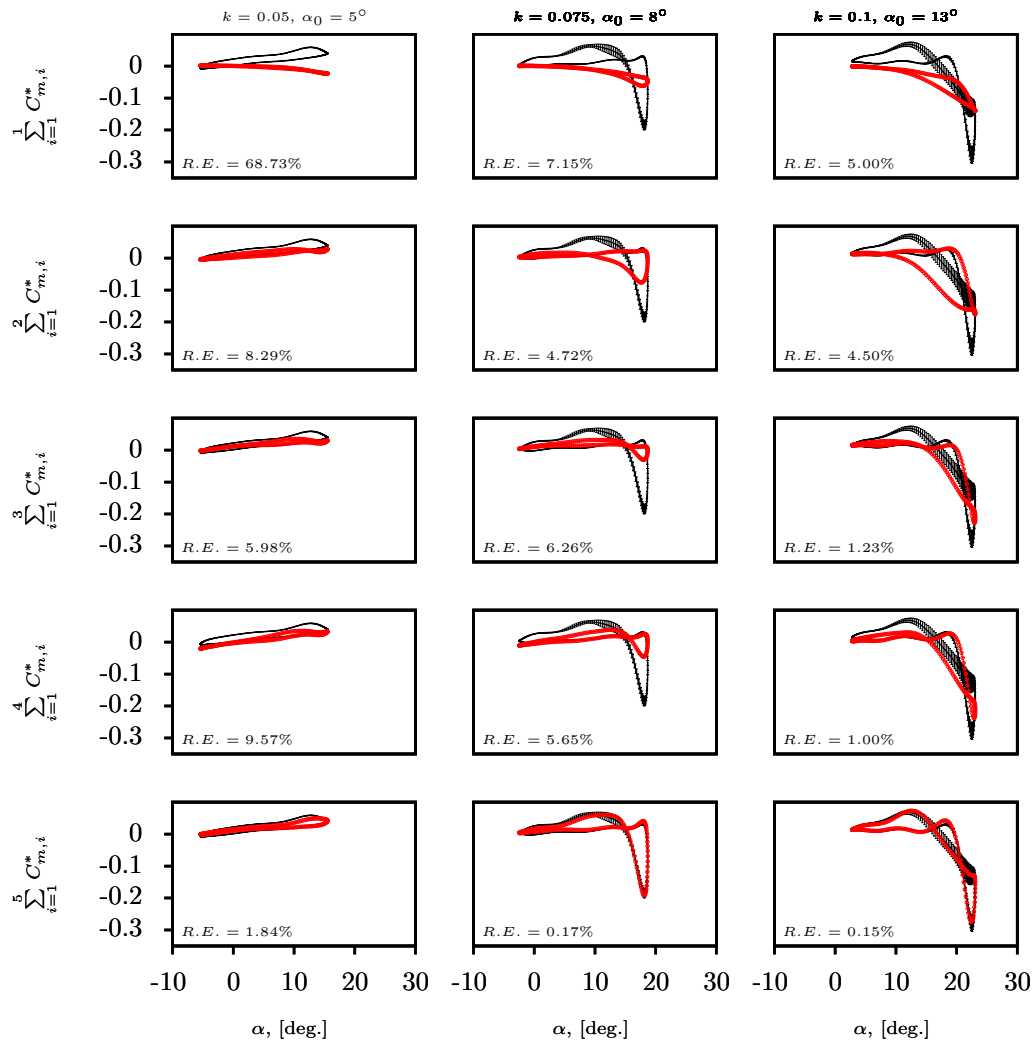American Institute of Aeronautics and Astronautics

Figure 12: Comparison of actual C_m^* to PPOD approximation of C_m^*:
Experiment $\perp$, PPOD ⊸

American Institute of Aeronautics and Astronautics

bulk of this distribution still resides toward the leading edge, yielding a distribution more appropriate for lift response manipulation.

Mode 1-4: The addition of mode 4 results in lift and moment reconstructions very similar to that of the three mode approximations. This behavior insists that while mode 4 may be important for the pressure field reconstruction, it does not significantly influence the integrated aerodynamic loads as can be seen by the small adjustments in the relative error. The shape of mode 4 in Figure 9 does not lend any further interpretations to this mode's contributions as it is noisy with most of its fluctuations occurring near the leading edge.

Mode 1-5: With the addition of mode 5 all of the important attributes of the integrated aerodynamic loads associated with dynamic stall appear to be captured. Namely, the angles of lift and moment stall are well defined as well as the moment stall magnitudes and flow reattachment angles. The change in lift curve slope due to the influence of the dynamic stall vortex is also captured as indicated by the rise in C_n^* in the $k = 0.1$, $\alpha_0 = 13°$ case at $\alpha \approx 20°$ on the upstroke. Because of this behavior, it is suspected that mode 5 is associated with the dynamic stall vortex, which is further supported by the mode shape in Figure 9. This mode shape provides a means of adjusting the lift and moment curves in response to a propagating structure over the upper surface of the airfoil.
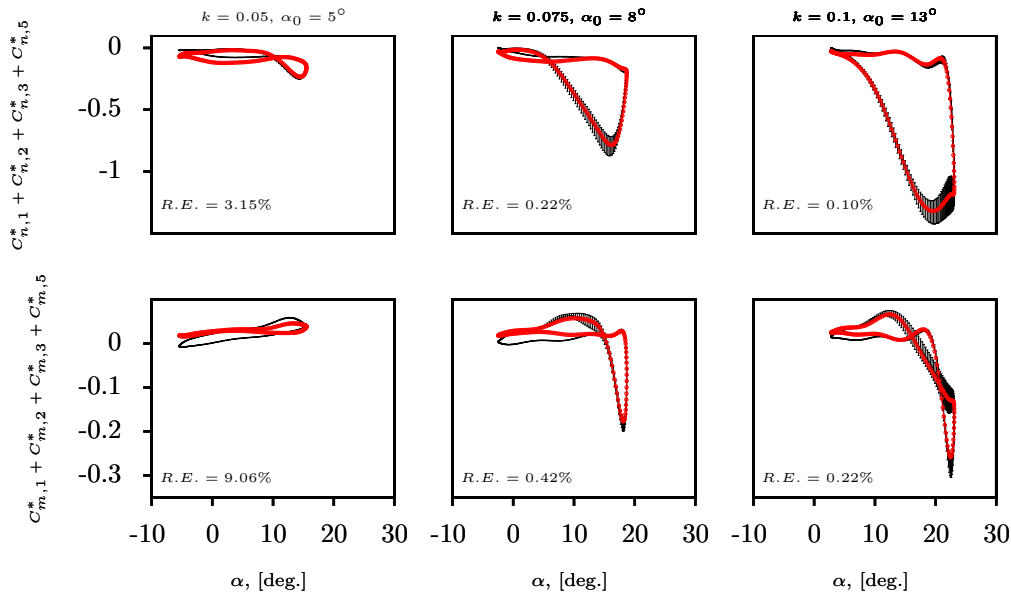

Figure 13: Four mode [1,2,3,5] comparison of aerodynamic loads to PPOD approximation: Experiment ⊥ , PPOD ─○─

In anticipation of creating a low-order model for the modal coefficients by a system of ordinary differential equations (ODEs), where it is highly advantageous to use as few modes as possible for the PPOD reconstructions, mode 4 is considered for exclusion because of its failure to exhibit an appreciable amount of contribution to the integrated aerodynamic load reconstructions. Figure 13 shows the PPOD approximations and their relative errors determined by considering only modes 1, 2, 3, and 5. Remarkably, the general features important to the dynamic stall process are still captured despite a slight increase in relative error for all cases compared to the five mode approximations. The most notable increase in relative error occurs for the integrated moment of the $k = 0.05$, $\alpha_0 = 5°$ case. However, as the mean angle of attack, α_0, increases, the PPOD approximations become much better, insisting that mode 4 is more important for lower angle of attack trajectories. For this reason, mode 4 is excluded from the reconstructions when considering the dynamics of the dynamic stall process due to its occurrence at higher angles of attack.

American Institute of Aeronautics and Astronautics

IV.C. Approximation of a Dynamical System

To further explore the behavior of the modal contributions to the surface pressure response during the dynamic stall process, a dynamical system is constructed by assuming that the time rate of change of the modal coefficients, $\mathrm{d}a_i/\mathrm{d}t$, are functions of the modal coefficients and parameters describing the pitching motion *i.e.* α, $\dot{\alpha}$, and $\ddot{\alpha}$. In an attempt to further include information about the airfoil shape, the stall penetration angle of attack, $\alpha_{sp} = \alpha - \alpha_{ss}$, is introduced to replace α. The pitch rate, $\dot{\alpha}$, and pitch acceleration, $\ddot{\alpha}$, terms are included because of their noticeable contributions from previous trials that will not be discussed here. The dynamical system of the modal coefficients then takes the following form:

$$\frac{\mathrm{d}\bar{a}}{\mathrm{d}t} \approx A\bar{a} + Q\bar{a}\bar{a} + T\bar{a}\bar{a}\bar{a} + F\bar{a}\bar{a}\bar{a}\bar{a} + B\bar{\eta} + R\bar{\eta}\bar{\eta} + U\bar{\eta}\bar{\eta}\bar{\eta} + G\bar{\eta}\bar{\eta}\bar{\eta}\bar{\eta} + C, \tag{20}$$

where A, Q, T, F, B, R, U, G, and C are constant matrices and tensors. The motion parameters are collected into the array $\bar{\eta} = [\alpha, \dot{\alpha}, \ddot{\alpha}]$. Higher order terms may be included but this analysis will only consider nonlinearities up to fourth order. The total influence of each parameter term in the expansion is determined from the magnitude of the coefficients of the constant matrices and tensors if the terms are normalized as

$$
\begin{aligned}
\frac{\mathrm{d}\bar{a}}{\mathrm{d}t} \approx\ & A\|\bar{a}\|_2 \left(\frac{\bar{a}}{\|\bar{a}\|_2}\right) + Q\|\bar{a}\bar{a}\|_2 \left(\frac{\bar{a}\bar{a}}{\|\bar{a}\bar{a}\|_2}\right) + T\|\bar{a}\bar{a}\bar{a}\|_2 \left(\frac{\bar{a}\bar{a}\bar{a}}{\|\bar{a}\bar{a}\bar{a}\|_2}\right) + F\|\bar{a}\bar{a}\bar{a}\bar{a}\|_2 \left(\frac{\bar{a}\bar{a}\bar{a}\bar{a}}{\|\bar{a}\bar{a}\bar{a}\bar{a}\|_2}\right) + \\
& B\|\bar{\eta}\|_2 \left(\frac{\bar{\eta}}{\|\bar{\eta}\|_2}\right) + R\|\bar{\eta}\bar{\eta}\|_2 \left(\frac{\bar{\eta}\bar{\eta}}{\|\bar{\eta}\bar{\eta}\|_2}\right) + U\|\bar{\eta}\bar{\eta}\bar{\eta}\|_2 \left(\frac{\bar{\eta}\bar{\eta}\bar{\eta}}{\|\bar{\eta}\bar{\eta}\bar{\eta}\|_2}\right) + G\|\bar{\eta}\bar{\eta}\bar{\eta}\bar{\eta}\|_2 \left(\frac{\bar{\eta}\bar{\eta}\bar{\eta}\bar{\eta}}{\|\bar{\eta}\bar{\eta}\bar{\eta}\bar{\eta}\|_2}\right) + \\
& C\|\bar{1}\|_2 \left(\frac{\bar{1}}{\|\bar{1}\|_2}\right),
\end{aligned}
\tag{21}
$$

where $\|\cdot\|_2$ is the L^2 norm of the terms constructed from the dataset values. This form will be abbreviated as

$$\frac{\mathrm{d}\bar{a}}{\mathrm{d}t} \approx \tilde{A}\breve{a} + \tilde{Q}\breve{a}^2 + \tilde{T}\breve{a}^3 + \tilde{F}\breve{a}^4 + \tilde{B}\breve{\eta} + \tilde{R}\breve{\eta}^2 + \tilde{U}\breve{\eta}^3 + \tilde{G}\breve{\eta}^4 + \tilde{C}\breve{1}. \tag{22}$$

Knowing the time rate of change of the modal coefficients from the experimental data, the normalized coefficients, $\widetilde{(\cdot)}$, are determined by considering a least-squares fit

$$\sum_{k,\alpha_0,\alpha_1} \int_t \left[\frac{\mathrm{d}\bar{a}}{\mathrm{d}t} - \left(\tilde{A}\breve{a} + \tilde{Q}\breve{a}^2 + \tilde{T}\breve{a}^3 + \tilde{F}\breve{a}^4 + \tilde{B}\breve{\eta} + \tilde{R}\breve{\eta}^2 + \tilde{U}\breve{\eta}^3 + \tilde{G}\breve{\eta}^4 + \tilde{C}\breve{1}\right)\right]^2 \mathrm{d}t \to min, \tag{23}$$

resulting in a set of ODEs describing the dynamical behavior of the modal coefficients as proposed by Ausseur and Pinier.[1] The modal coefficients are determined for the global system *i.e.* using all the cases for the least-squares fit, or a local fit is made by excluding certain cases. For this paper, only approximations determined from the global system are considered. The ODEs are integrated in time using the initial conditions $\{a_i(t/T = 0)\}$ to yield the modeled coefficient trajectories. Figure 14 depicts an example of the ODE approximation (left) and the integrated modal coefficient values (right) for the $k = 0.1$, $\alpha_0 = 13°$, deep stall case. It is clear that the fourth order approximation is more than capable of predicting the behavior of the time rate of change of each mode despite the highly oscillatory response. However, the resulting modal coefficients experience difficulty in continuity at the beginning and end of the pitching cycle (the minimum angle of attack) as seen in the center column of Figure 14. This issue arises because of the time-stepping nature of the integration and slight errors in the approximations of they system. Because the pitching motion is harmonic, the modal coefficients should be the same at $\alpha(t/T = 0)$ and $\alpha(t/T = 1)$, where T is the cycle period. For this reason, each modal coefficient is expressed as a combination of the rate function, $\mathrm{d}a_i/\mathrm{d}t$, integrated forward in time and backwards in time,

$$a_i(t) = w_1(t) \int_0^t \frac{\mathrm{d}a_i(\xi)}{\mathrm{d}\xi}\mathrm{d}\xi + w_2(t) \int_T^t -\frac{\mathrm{d}a_i(\xi)}{\mathrm{d}\xi}\mathrm{d}\xi, \tag{24}$$

American Institute of Aeronautics and Astronautics

where w_x are weighting functions defined by

$$
\begin{aligned}
w_1 &= \frac{1}{2}\left(1 + \cos(\pi * t/T)\right), \\
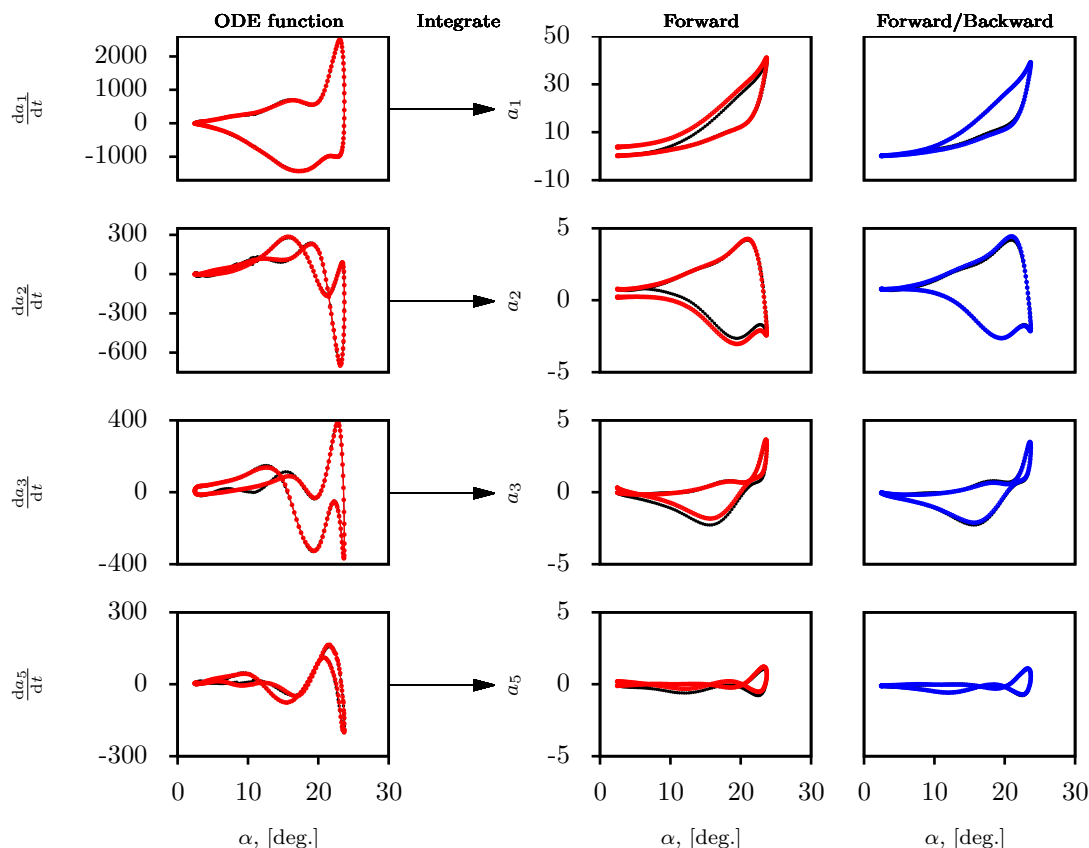w_2 &= \frac{1}{2}\left(1 - \cos(\pi * t/T)\right).
\end{aligned}
\tag{25}
$$

Figure 14: 4th order dynamical system for $k = 0.1$, $\alpha_0 = 13°$:
PPOD —•— , 4th order estimate —○— , Corrected Integration —○—

Figure 15 further clarifies this integration scheme showing the direction of integration and respective weighting function profiles. By implementing the weighting functions, time stamps at the beginning of the trajectory are dominantly derived from the forward integration while time stamps towards the end of the trajectory are constructed from the backwards integration. In this way, the values of the modal coefficients at the beginning and end of the pitching cycle can be guaranteed to be equivalent. The resulting corrected integrated values are shown in the right column of Figure 14. Accuracy of the prediction is improved over the forward integration method and continuity of the end points is achieved.

Using the fourth order approximation for the dynamical system results in 104 normalized coefficients for each modal coefficient. The relative magnitudes of these normalized coefficients, defined as $|\breve{c}|/\sum|\breve{c}|$, are used to determine which parameters are more significant to the modal behavior. Figure 16 and Figure 17 show the relative contributions of the modal parameters, $\bar{a}$, and the motion parameters, $\breve{\eta}$, respectively, for each mode in the fourth order global approximation. These figures are organized as bar plots where the largest magnitude at each parameter location is pushed to the background and smaller magnitudes are ordered to the foreground so that the peak value for each mode is visible. The largest contribution parameter for each
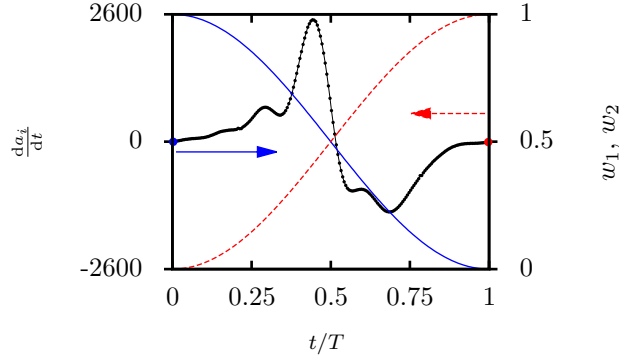
American Institute of Aeronautics and Astronautics

Figure 15: ODE integration scheme:
ODE function $\rightarrow$, w_1 — , w_2 - -

mode is as follows: mode 1 = $a_1^2 a_5$ (9.45%), mode 2 = a_1^2 (9.30%), mode 3 = a_1^3 (14.37%), and mode 5 = a_1^2 (7.78%). In the global estimation each mode exhibits a strong nonlinear dependence on mode 1. In fact, the local peak clusters in Figure 16 all occur around the mode 1 dominated contributions. The only modes significantly influenced by motion parameters are modes 1 and 2 with nearly all of the contributions coming from α_{sp} terms (denoted as α in Figure 17).

V.   Conclusions

The unsteady surface pressure field of a NACA 23012 airfoil pitching in an incompressible flow has been decomposed using a parametric proper orthogonal decomposition. By using multiple pitching trajectories for the decomposition, spatial mode shapes were determined that are generic to the entire set of pitching parameters *i.e.* adequately capture the dynamic behavior of attached flow pitching, light stall, and deep stall. The energy convergence of the decomposition was rapid enough that the integrated aerodynamic loads were appropriately reconstructed with as few as four modes. From these four modes a low-order dynamical system was developed to elucidate the influence of each mode and pitching parameter on the behavior of the modal coefficients. It was found that the time rate of change of each modal coefficient is well approximated with a fourth order expansion. The normalized coefficients of the expansion were determined using a least-squares fit of the entire set of pitching parameters (global approximation). With the appropriate initial conditions and integration scheme, the modal coefficients were well approximated. Comparison of the relative magnitudes of the normalized expansion coefficients showed a high nonlinear dependence of each mode on mode 1. It was also shown that mode 1 and mode 2 were the only modes appreciably influenced by motion parameters in a global approximation.
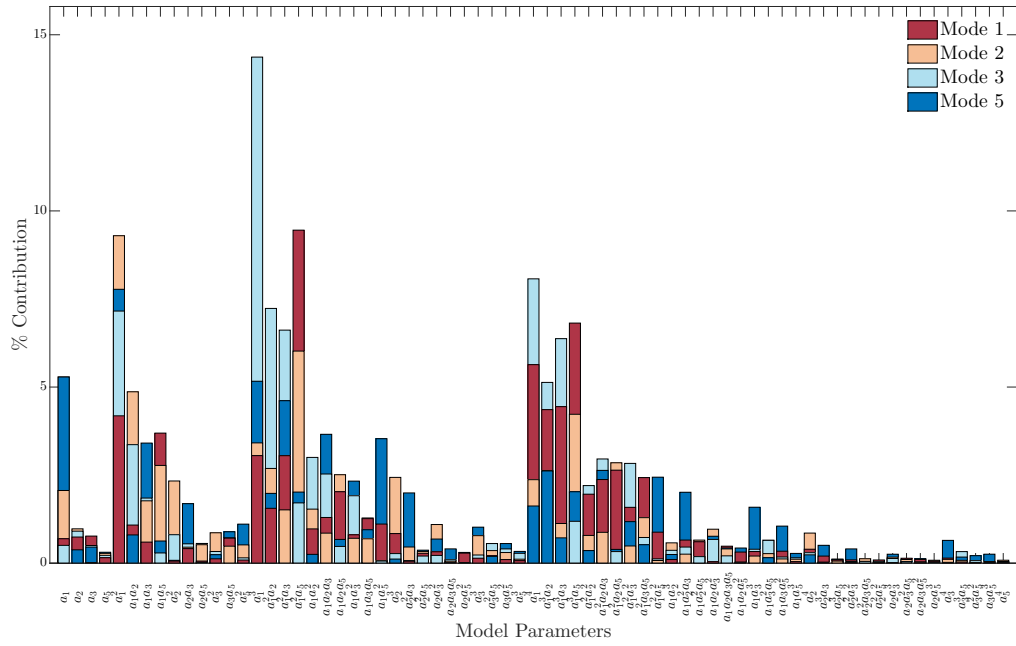
American Institute of Aeronautics and Astronautics

Figure 16: Contribution of modal parameters in global estimate
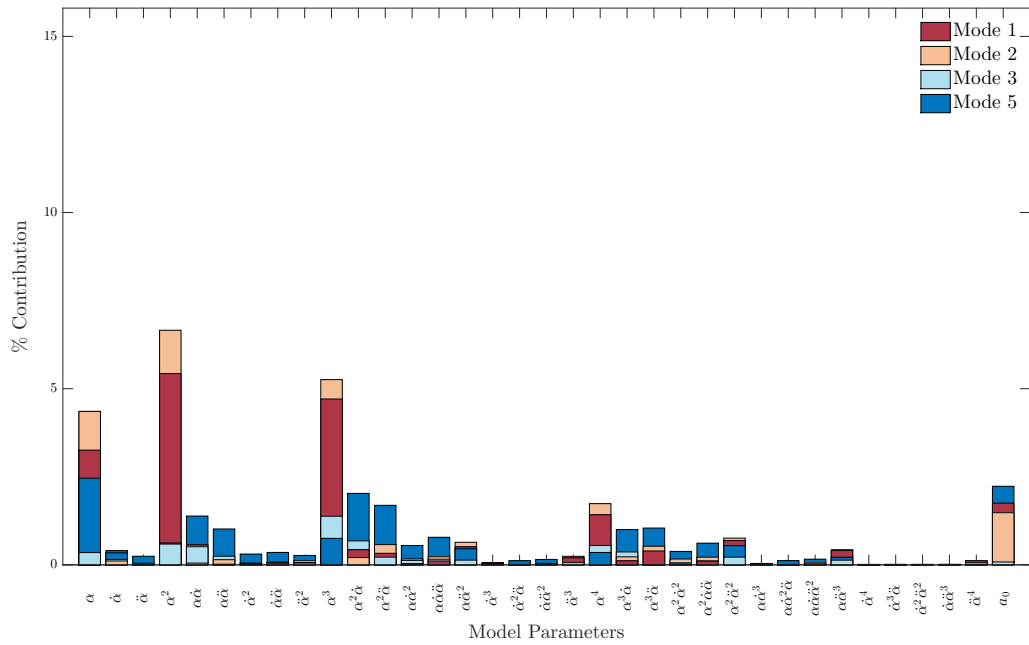
Figure 17: Contribution of motion parameters in global estimate

American Institute of Aeronautics and Astronautics

References

[1] Julie M. Ausseur and Jeremy T. Pinier. Towards closed-loop feedback control of the flow over naca-4412 airfoil. In *43rd AIAA Aerospace Sciences Meeting and Exhibit*, Reno, Nevada, January 10-13 2005. AIAA.

[2] L. W. Carr. Progress in analysis and prediction of dynamic stall. *Journal of Aircraft*, 25(1):6–17, January 1988.

[3] T. Cebeci, K.-C. Chang, H. Chen, M. Platzer, and J. P. Shao. *Analysis of Low-Speed Unsteady Airfoil Flows*. Horizons Pub., 2005.

[4] L. E. Ericsson and J. P. Reding. Unsteady airfoil stall. Technical Report NASA CR-66787, NASA, July 1969.

[5] S. Gordeyev and F. O. Thomas. A temporal proper decomposition (tpod) for closed-loop flow control. *Experiments in Fluids*, 54(3):1–16, 2013.

[6] P. Holmes, J. L. Lumley, G. Berkooz, and C. W. Rowley. *Turbulence, coherent structures, dynamical systems and symmetry*. Cambridge University Press, 1998.

[7] J. Gordon Leishman. *Principles of Helicopter Aerodynamics*. Cambridge University Press, 2000.

[8] J. L. Lumley. *Stochastic tools in turbulence*. Applied mathematics and mechanics. Academic Press, 1970.

[9] W. J McCroskey, K. W. McAlister, L. W. Carr, S.L. Pucci, O. Lambert, and R. F. Indergrand. Dynamic stall on advanced airfoil sections. *Journal of the American Helicopter Society*, 26:40–50, 1981.

[10] W. J. McCroskey and S. L. Pucci. Viscous-inviscid interactions on oscillating airfoils in subsonic flow. *AIAA Journal*, 20(2):167–174, 1982.

[11] W.J. McCroskey. The phenomenon of dynamic stall. Technical report, NASA, March 1981.